scientific reports

Check for updates

OPEN

Acoustic emission monitoring reveals keyhole formation and evolution

Louis Galiègue[1]✉, Fabien Briffod[2], Kaita Ito[2], Hiroshige Masuo[3], Makoto Watanabe[2], Takayuki Shiraiwa[1] & Manabu Enoki[4]

We present results from airborne acoustic emission (AE) monitoring during the Laser Powder Bed Fusion (LPBF) process. A distinct acoustic signature was consistently observed alongside keyhole formation and plume instability, with its frequency inversely proportional to the depth of the melt pool. The effects of laser scanning speed, laser power, material (Ti–6Al–4V, S316L, Inconel625), and laser spot size on AE signals were systematically investigated. A resurgence of high-frequency components for deep melt pools was found to coincide with the onset of keyhole-induced porosity. This acoustic signature is attributed to fluctuations at the liquid–vapor interface, which drive oscillations in the vaporization plume. Multi-track experiments further demonstrated the potential of AE monitoring for real-time fault detection and closed-loop process control in LPBF.

Laser Powder Bed Fusion (LPBF) is a widely employed metal Additive Manufacturing (AM) process that enables the fabrication of complex geometries and innovative design solutions, leading to mass reduction, cost savings, and shorter lead times. Decades of extensive research have matured LPBF to a level suitable for demanding high-end applications in sectors such as aerospace[1] and medical implants[2].

Different melting regimes can be reached during fabrication, eventually leading to defect formation. At lower energy densities, a stable, shallow melt pool forms in the conduction mode. As energy density increases, a transition to keyhole mode may occur. This regime is characterized by intense vaporization, forming a deep, narrow vapor cavity that enhances laser absorptivity through multiple reflections at the liquid-vapor interface. Although the keyhole regime achieves greater penetration depths, its inherent complexity and instability can lead to collapse, entrapping gas and generating porosity within the fabricated part[3].

The mechanisms underpinning keyhole formation[4] and its role in porosity generation[5–7] have been extensively investigated, notably through in-situ synchrotron imaging. These observations have led to the development of scaling laws[8–10] that predict the conduction-to-keyhole transition across various materials and laser parameters.

However, such scaling laws are not sufficient to guarantee the production of defect-free parts. In-process instabilities can still arise even under nominally stable process parameters due to factors such as local surface roughness, angle-dependent laser absorptivity (Fresnel absorption), and thermal accumulation influenced by part geometry and scanning strategy[7,11,12]. Consequently, mandatory post-processing heat treatments are applied to relieve thermal stresses and reduce fabrication-induced porosity[13].

While post-processing can mitigate some defects, it neither addresses their origin nor prevents their initial occurrence. For applications requiring high reliability, there is a growing demand for real-time, in-situ monitoring solutions capable of detecting process instabilities as they emerge, potentially enabling closed-loop control. Various sensing techniques have been explored to monitor the LPBF process in real time, including optical[14,15], thermal[16,17] and Acoustic Emission (AE)[11,18–21] monitoring, which are in most studies coupled with machine learning processes. Although these machine-learning aided monitoring methods yield great results in defect or melting regime identification, their generalization across different process parameters and setups are not trivial. Integrating physical insight into AI-driven models has been shown to improve both performance and robustness[17], ultimately contributing to more reliable and interpretable monitoring systems.

The physical origin of specific AE signals during keyhole-mode melting is not yet fully understood. The formation of a vapor cavity can generate a variety of acoustic signals, including solid-state elastic waves associated

[1]Department of Materials Engineering, The University of Tokyo, 7-3-1 Hongo, Bunkyo-ku, 113-8656 Tokyo, Japan. [2]Research Center for Structural Materials, National Institute of Materials Science, 1-2-1 Sengen, Tsukuba, Ibaraki 305-0047, Japan. [3]Metal Technology Co. Ltd., 5-4-14 Shake, Ebina 243-0424, Japan. [4]Katayanagi Advanced Research Institute, Tokyo University of Technology, 1404-1 Katakuramachi, Hachioji City, Tokyo 192-0982, Japan. ✉email: galiegue.lg@gmail.com

with phase transformations[22], pressure fluctuations from impinging vapor jets[22], forced oscillations of the vapor cavity[23], transient chamber resonances[21], and oscillations of the primary vaporization site[24].

Acoustic frequencies characteristic of keyhole-mode operation have been reported in the 40–80 kHz range[11,19,21], becoming increasingly chaotic and broadband for deeper, unstable keyholes. While broadband emission is consistent with chaotic behavior, the considerable variability in reported frequency peaks across different studies for stable keyholes suggests a dependence on process conditions. Indeed, despite being classified under the same melting regime, keyholes can exhibit radically different vapor cavity geometries in terms of depth, length, and width[4], which may produce distinct AE signatures. Liquid-vapor boundary oscillations have also been studied, both experimentally[4,6] and numerically[24,25] leading to a understanding of the mechanisms of porosity formation in unstable keyholes.

The aim of the present study is to provide physical insight into the AE signature of the keyhole regime. We observe that a distinct acoustic frequency emerges concurrently with the transition from conduction to keyhole mode. Single-line scans were performed across a broad range of process parameters on bare substrates of three different materials: Ti–6Al–4V, S316L stainless steel, and Inconel 625. The AE was recorded using a microphone sensitive in the 2–200 kHz range. Melting regimes were identified through post-mortem cross-sectional analysis of the melt pool, while porosity formation was characterized using X-ray computed tomography (XCT).

Results and discussion

Onset of instabilities during keyhole formation

During laser-based additive manufacturing, the transition from conduction to keyhole mode is critical to ensure defect free fabrication. As the laser energy density increases, a sharp transition to keyhole mode occurs, driven by multiple internal reflections of the laser beam within the cavity, which intensify energy absorption and deepen the vapor cavity[3,4]. The steep thermal gradients at the melt pool surface induce significant surface tension variations, which drive Marangoni convection[26]. These flow patterns, combined with recoil pressure from vaporization and capillary forces, govern the overall melt pool dynamics[27]. Concerning the vapor phase, increased vaporization under keyhole conditions generates a prominent plume, whose direction is typically normal to the front wall of the keyhole[28].

Figure 1 illustrates the evolution of melt pool cross-section and surface morphology during the transition from conduction to shallow keyhole mode for a Ti–6Al–4V bare-substrate line scan. At lower power (Fig. 1a, b), the melt pool exhibits a characteristic semi-circular profile associated with conduction mode with a homogeneous surface. As laser power increases (Fig. 1c, d), the melt pool deepens while maintaining its shape, and the surface remains mostly uniform, with only occasional chevron-like patterns appearing along the track. At even higher power (Fig. 1e,f) the shape of the melt pool deviates from the semi-circular geometry, signaling the onset of shallow keyhole mode. In this regime, regular chevrons form on the surface, tracing the solidification front[29]. These features are indicative of melt pool instabilities, which cause fluctuations in solidification height.

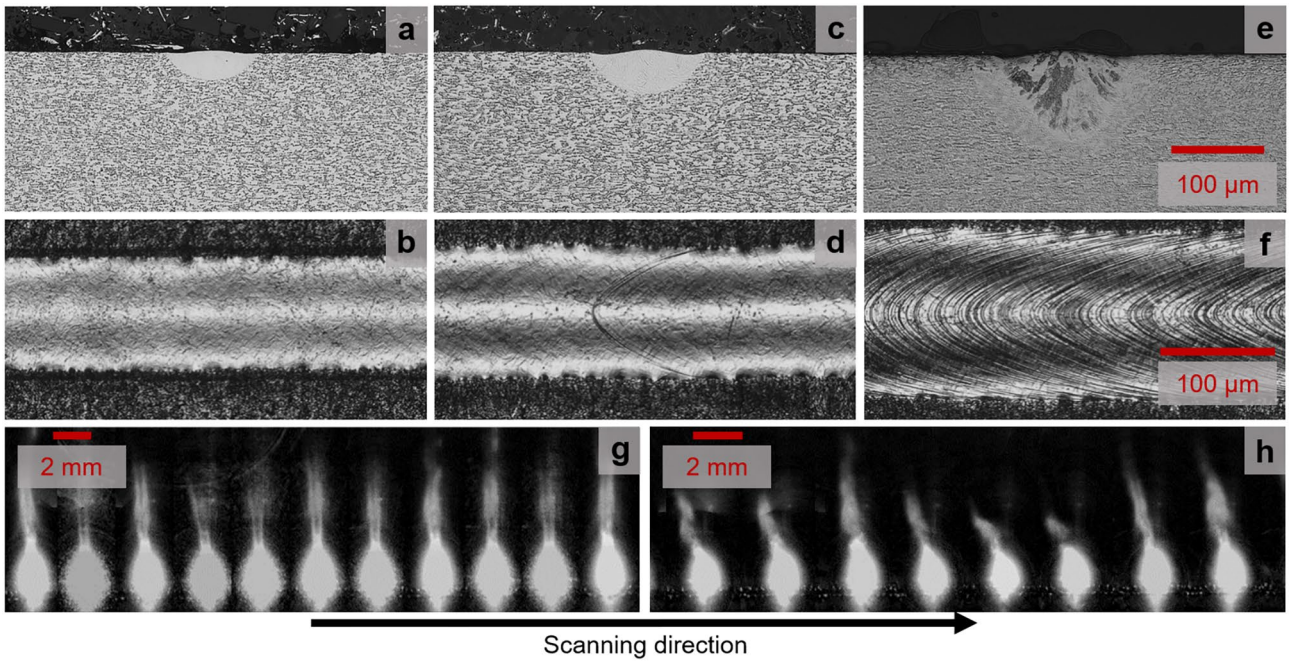

Fig. 1. Line track cross-sections and surface observations for Ti–6Al–4V at a scan speed of 400 mm/s under varying laser powers. **(a, b)** 60 W – conduction mode; **(c, d)** 80 W – conduction mode; **(e, f)** 100 W – transition to keyhole mode. **(g, h)** High-speed imaging of the plume during conduction **(g)** and keyhole **(h)** regimes. The camera operated at 10,000 fps with an exposure time of 10 μs, dynamically reduced to 2 μs in cases of overexposure. Each shown frame is separated by 3 ms.

High-speed imaging was conducted to capture plume behavior under both melting conditions. The camera was focused on a single scan track at an angle of approximately 30° relative to the substrate surface and recorded at a frame rate of 10,000 frames per second (fps). The resulting image sequences were processed to mitigate glare and transient reflections (see Methods for details). Fig. 1g and h present selected frames arranged sequentially, with a time interval of 3ms between each. In conduction mode (Fig. 1g), the plume appears nearly vertical and remains stable over time. In contrast, under keyhole conditions (Fig. 1h, and Supplementary Fig. S1), the plume exhibits unstable behavior, inclining toward the horizontal and oscillating in both direction and length. As the energy density increases, the front wall of the keyhole gradually tilts toward the vertical[30]. Since the plume is oriented perpendicular to the evaporation surface[28], it correspondingly rotates toward the horizontal direction.

As noted in previous studies[4], a small vapor cavity is already present during conduction-mode melting. The stability of the plume in this regime indicates that the vaporization process remains steady. However, once the transition to keyhole mode begins and the vapor cavity reaches a sufficiently large volume, plume instabilities and a slight inclination become apparent. These oscillations are understood to originate from instabilities at the vaporization front, where the liquid–vapor interface oscillates due to the dynamic interplay between recoil pressure–which promotes cavity expansion–and capillary forces, which act as a restoring mechanism.

Acoustic signature of keyhole formation

Scanning conditions were selected to encompass the transition from conduction mode to keyhole formation. AE signals were primarily analyzed using the Continuous Wavelet Transform (CWT) to provide a time–frequency representation. To ensure analysis focused on a well-established melting regime, the first and last quarters of the irradiation period were excluded. Local maxima in the CWT were identified and marked as black dots to highlight significant AE events.

Figure 2 illustrates the evolution of AE activity with increasing energy density, alongside corresponding post-mortem cross-sections of the melt tracks. In the conduction regime (Fig. 2a), the melt pool exhibits a characteristic shallow, semi-circular shape. The associated AE activity is concentrated between 5 and 15 kHz, with only a few transient peaks. As the process transitions to keyhole mode (Fig. 2b), the melt pool assumes a more elongated geometry with a higher aspect ratio. This change is also reflected in the CWT, where numerous transient events emerge around 80 kHz, superimposed on the low-frequency background observed in conduction

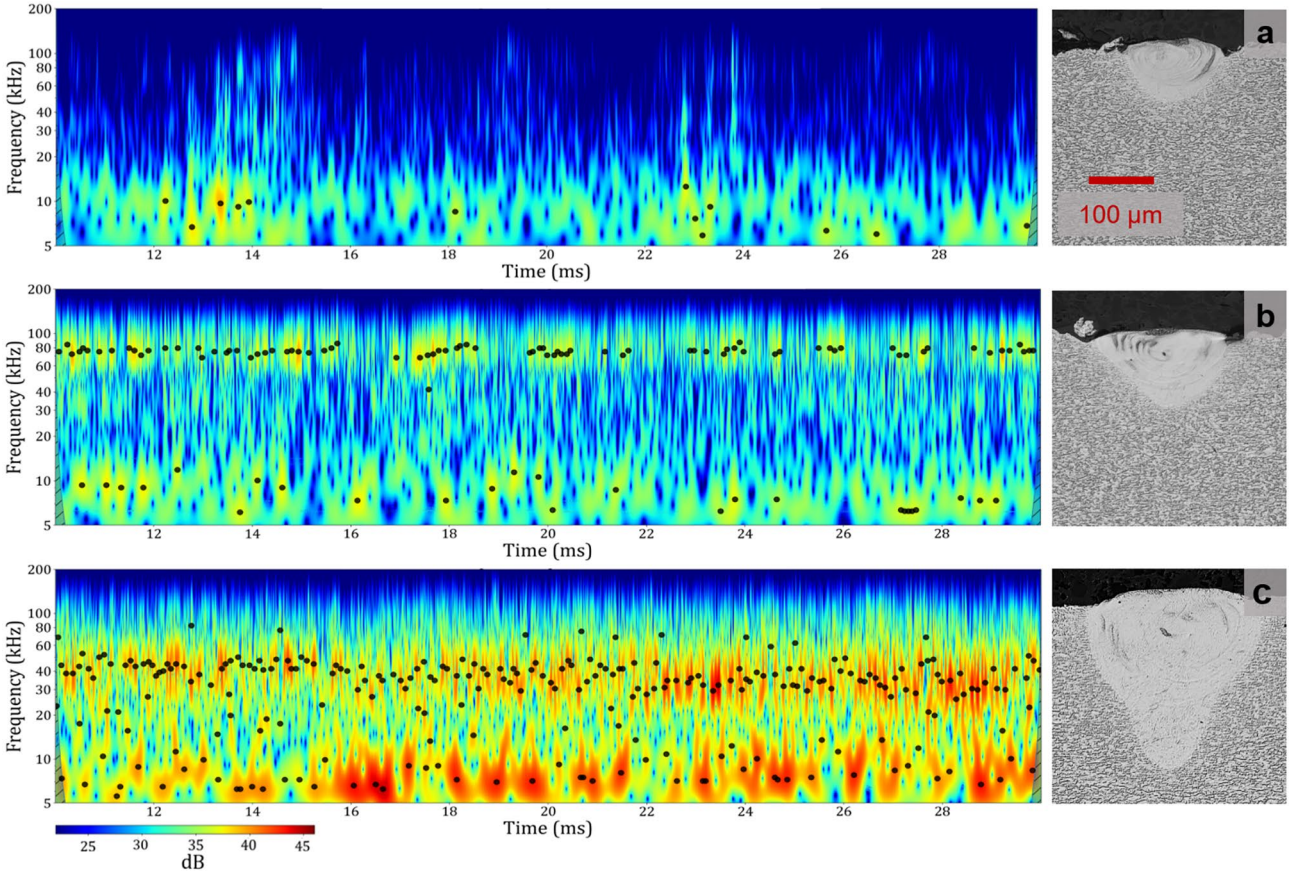

Fig. 2. Continuous Wavelet Transform (CWT) of the recorded signals and corresponding melt pool cross-sections for single track experiments conducted at a scanning speed of 250 mm/s on a Ti–6Al–4V substrate. Local maxima in the CWT are indicated by black dots. **(a)** 80 W – conduction mode; **(b)** 100 W – transition to keyhole; **(c)** 130 W – keyhole mode.

mode. With further increases in energy density (Fig. 2c), the melt pool deepens, and the AE activity shifts to a broader, lower frequency range, approximately 25 to 40 kHz. A broader set of observations is provided in Supplementary Figure S2.

To understand the origin of airborne acoustic emission (AE), we synchronized the CWT scaleogram with high-speed imaging footage. A representative example for a single-track scan at 150 mm/s and 120 W is shown in Figure 3 and Supplementary Video F1. This specific scan was realized with high surface roughness caused by a previous pass at the same location. We focus on a 100 ms time window, starting after the melting regime is expected to be fully established, to observe potential in-process instabilities. Specific frames from the high-speed video were extracted to illustrate the plume morphology at selected time points.

At time $t_1 = 70.9$ ms, the plume appears vertical but unstable, oscillating in an S-shaped pattern. The corresponding CWT shows strong activity above 20 kHz, with a pronounced peak near 40 kHz. The broad range of frequencies is attributed to a highly unstable keyhole due to the rough surface in this specific scan. At $t_2 = 95.3$ ms, the plume behavior changes abruptly, becoming stable and laminar. This transition is accompanied by a marked decrease in AE amplitude across all frequencies. Similar transitions in plume behavior and AE reduction were observed at $t_3 = 117.4$ ms and $t_4 = 121.8$ ms.

These in-process instabilities, leading to different melting regimes for identical process parameters, are both identified through high-speed imaging and AE recording. In conduction mode, although a shallow vapor cavity may already exist–as evidenced by the presence of faint fumes–the flow remains stable and laminar, producing little to no AE. In contrast, as the process enters transition mode, the flow becomes unstable and exhibits vortex shedding patterns, which coincide with significant AE activity.

Based on these observations, a systematic study was conducted across varying scanning speeds and laser powers to quantify the emergence and shift of this characteristic acoustic signature as the melt pool deepens. For clarity, this characteristic frequency will be referred to as the keyhole frequency throughout the remainder of the text. As energy density increases, the keyhole frequency spans a broader range, making it more challenging to assign a single representative value. To address this, local maxima were extracted from each CWT, and the keyhole frequency was defined as the median value within the frequency band of interest (see Methods for details).

Figure 4 presents the evolution of the keyhole frequency as a function of melt pool depth (denoted as e) under various low-speed conditions (referred to as V). Several key observations can be drawn from this data: the keyhole frequency consistently appears across all scanning speeds, tends to saturate at approximately 20kHz under high energy density conditions, and exhibits an inverse relationship with shallow melt pool depth. Notably, identical melt pool depths do not consistently yield the same acoustic response when achieved through different process parameters. Specifically, at equal melt pool depth, a higher scanning speed correlates with a lower emitted frequency. However, when corrected by a factor proportional to the square root of the scanning

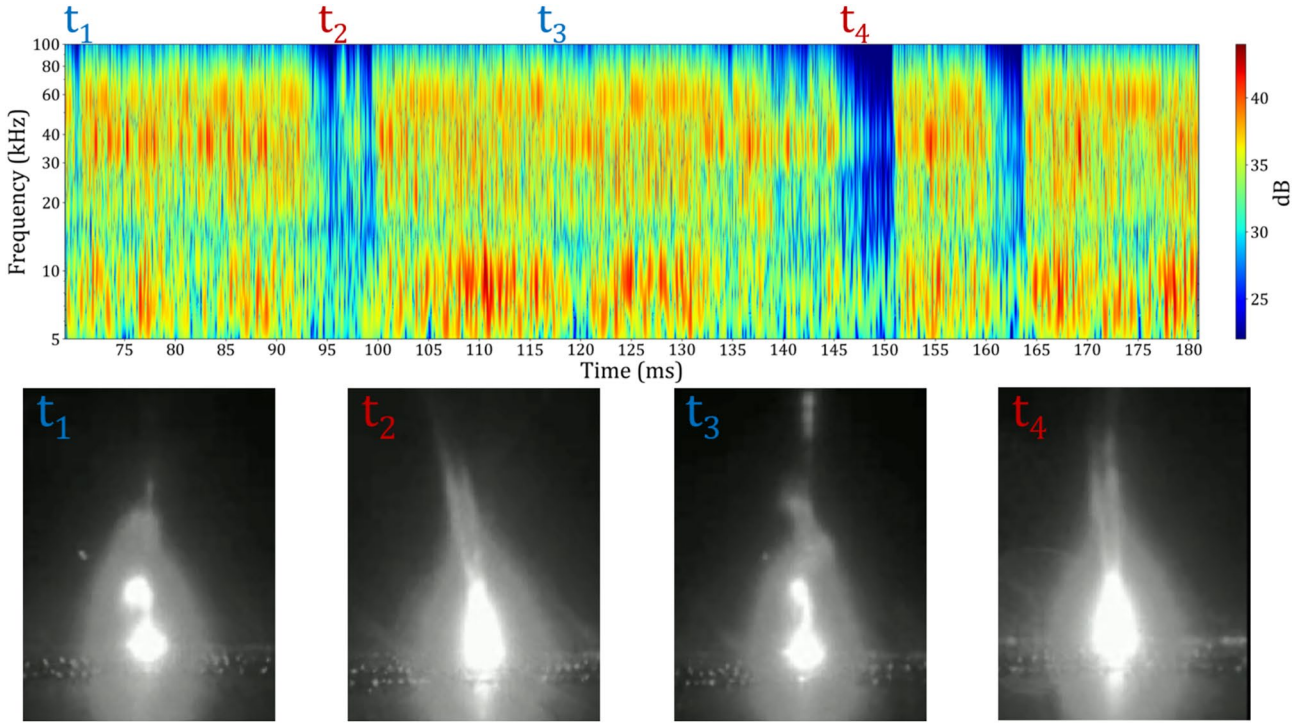

Fig. 3. CWT of Ti–6Al–4V substrate, 150 mm/s, 120 W line track compared with synchronized frames of high speed imaging. $t_1 = 70.9$ s, $t_2 = 95.3$ s, $t_3 = 117.4$ s and $t_4 = 148.5$ s. Frames are extracted from Supplementary Video F1.

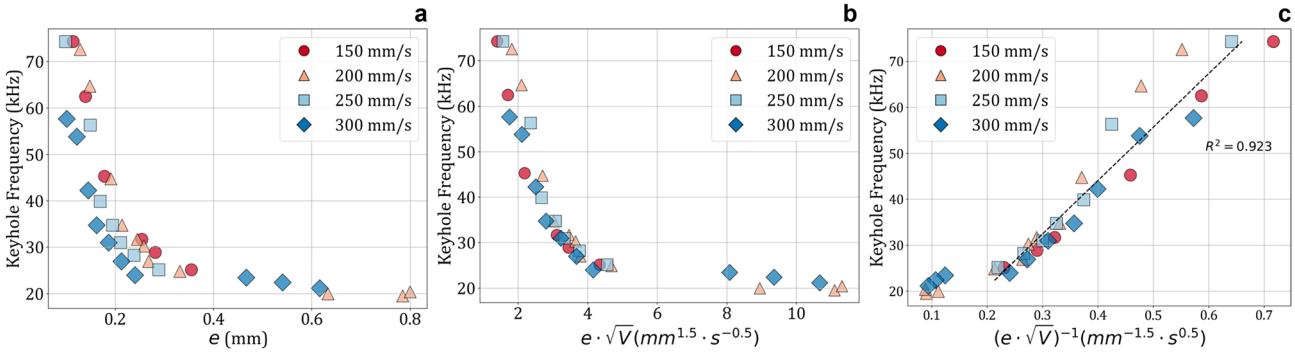

Fig. 4. Keyhole frequency against melt pool depth **(a)**, melt pool depth multiplied by square root of scanning speed **(b)**, and the inverse of this product along with the corresponding linear regression **(c)** for single track experiments conducted on a Ti–6Al–4V substrate. The melt pool depth is averaged at 3 different point of each line scan.

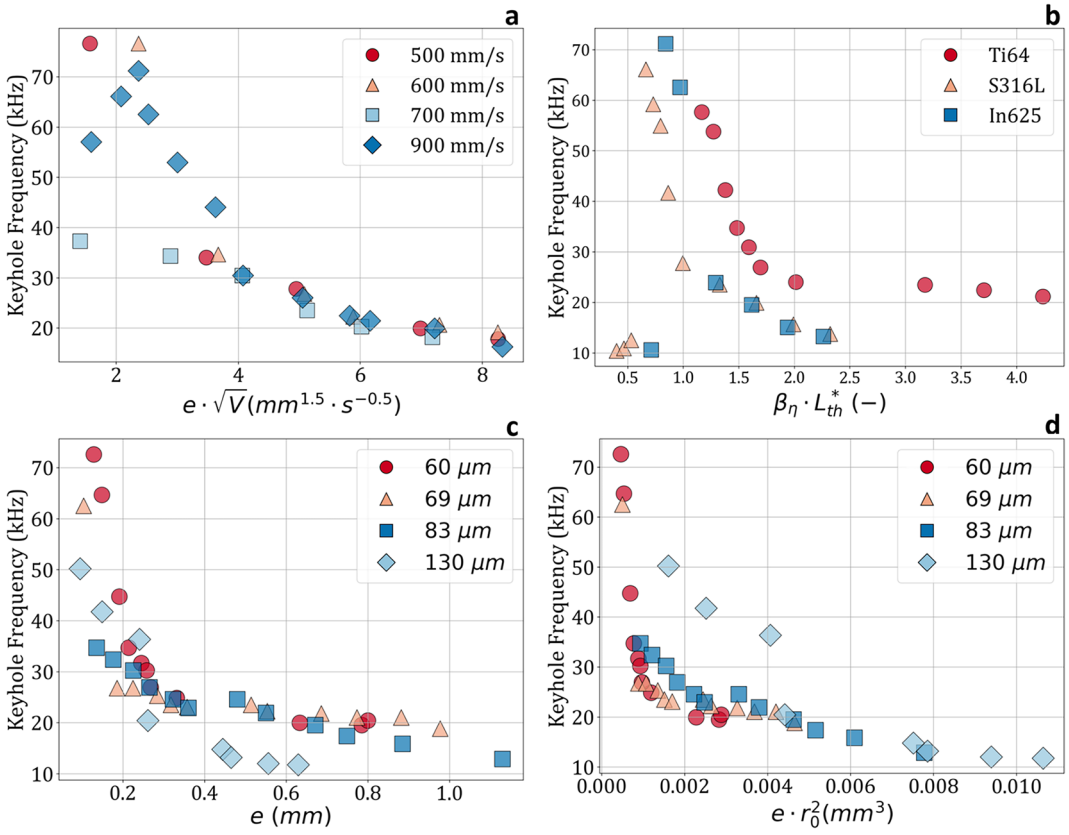

Fig. 5. Keyhole frequency evolution under different parameters. **(a)** At high scanning speed, against melt pool depth multiplied by square root of scanning speed. **(b)** Comparison across different materials plotted against $\beta_\eta \cdot L^*_{th}$ for a constant 300 mm/s scanning speed. **(c)** Effect of different laser spot sizes (radii), adjusted via laser defocusing for a constant 200 mm/s scanning speed.**(d)** Relationship with cavity volume estimation for different radii. The substrate is Ti–6Al–4V for (a,c,d).

speed (which also scales with laser power for equal reduced melting enthalpy[8]), all data point collapse into a single trend, as seen in Fig. 4b, which fits an inverse relationship (Fig. 4c).

The appearance and evolution of the keyhole frequency were further investigated at higher scanning speeds (500–900 mm/s), using different materials (Ti–6Al–4V, Inconel625, and S316L stainless steel), and with varying laser spot sizes obtained via negative defocus (i.e., with the beam waist located inside the material). The results are presented in Fig. 5.

Conditions with higher scanning speeds, which are more representative of typical LPBF parameters, also exhibited the characteristic keyhole frequency. Notably, the onset of keyhole formation was found to be unstable

under low-power conditions, with significant fluctuations in the AE signal amplitude within a single scan line (see Supplementary Fig. S4). This instability aligns with previous observations that the LPBF melting regime can remain unstable even under constant process parameters, particularly near the boundary of keyhole formation[11]. Once a stable melting regime is established, Fig. 5a shows that the relationship between keyhole frequency and melt pool depth remains consistent with the trends observed at lower scanning speeds.

For different materials, scaling laws have been established to predict the normalized melt pool depth, $e^* = \frac{e}{r_0}$ through the product of the reduced melting enthalpy β_η and the normalized thermal diffusion length L^*_{th}[9] (see Supplementary Fig. S3):

$$\frac{e}{r_0} = \beta_\eta L^*_{\text{th}} = \frac{\eta(P,V)\,P}{\pi(T_m - T_0)\,\rho C_p \sqrt{\alpha V r_0^3}} \sqrt{\frac{\alpha}{r_0 V}} \tag{1}$$

where ρ is the liquid-state density, C_p the specific heat capacity, T_m and T_0 the melting and substrate temperatures, α the thermal diffusivity, V the scanning speed, r_0 the laser radius, P the laser power, and η the absorptivity.

The absorptivity depends on the process conditions P and V, and is expressed as:

$$\eta(P,V) = 0.7\left(1 - e^{-0.6\beta_{\eta_m} L^*_{\text{th}}}\right) \tag{2}$$

where η_m denotes the minimum absorptivity recorded during line scans[9]. All thermal properties used for calculation are taken at the melting temperature and are listed in Supplementary Data 1. Keyhole frequency for three different materials was also observed and results are presented in Fig. 5b against $\beta_\eta \cdot L^*_{th}$.

All three materials exhibited a high frequency at the transition. Interestingly, Ti–6Al–4V experiment showed a higher frequencies for deep keyholes compared to Inconel625 and S316L suggesting a material-dependent signature for deep keyholes. Evidence of a material-dependent variation in keyhole oscillation frequency has not been reported in the literature, and surface tension alone cannot account for this difference. Indeed, the respective surface tension coefficient for Ti–6Al–4V, Inconel718 and S316L do not present a comparable order: $\sigma_{Ti64} = 1.50$ N/m[31], $\sigma_{In718} = 1.88$ N/m[32] and $\sigma_{S316L} = 1.59$ N/m[33]. Further investigation is required to explain this observation.

Finally, the impact of different laser spot sizes, achieved through laser defocusing, was investigated. In these experiments, the sample was positioned above the laser focal point, causing the beam to focus inside the material. While this setup allows for varying spot sizes, it is important to note that the resulting melting regime differs for identical laser beam sizes depending on positive or negative defocus distances[34]. Results are shown in Fig. 5c. Similar behavior is observed throughout all laser beam spot size, but bigger radii led to lower frequencies, at both low depth and high depth keyholes. Indeed, if plotted against the cavity estimated volume $\Omega \propto e \cdot r_0^2$, all curves collapse into one (Fig. 5d).

Experiments with highly defocused beams ($r_0 = 130$ μm) exhibited unstable behavior at low laser powers: the keyhole frequency fluctuated significantly along the scanning track during irradiation (see Supplementary Fig. S5). This instability is believed to result from the laser beam waist being located inside the material. While such a configuration can enhance energy absorptivity during the transition to deeper vapor cavities, it may not provide sufficient energy to sustain the cavity, leading to its collapse and corresponding acoustic instability.

In this study, experiments were conducted both within an argon atmosphere and in the absence of shielding gas. The observations under both conditions showed no discernible variation in acoustic keyhole frequency, all other parameters being equal.

Intrinsic keyhole oscillation of the liquid-vapor boundary have been identified through thermal imaging, high-speed synchrotron imaging, and simulations[17,25]. This oscillation frequency is governed by a balance between Marangoni forces, recoil pressure, and surface tension, and is believed to be responsible for the observed acoustic keyhole frequency. Consistent with our experimental results, simulations revealed thermal intensity oscillations ranging from approximately 40 kHz at high scanning speeds to 16 kHz at lower speeds, under constant laser power. Notably, these oscillations involve a periodic shift of the main vaporization point being either on the front or on the rear wall of the keyhole, which contributes to plume destabilization. While the frequency relationship with process parameters has been identified, the physical mechanisms governing the evolution of this keyhole acoustic frequency with the melting regime remain to be fully understood. A comprehensive physical or numerical model is missing, and further theoretical development is needed.

Insight onto keyhole porosity

The transition from conduction mode to a shallow keyhole revealed the emergence of a distinct high-frequency acoustic signal, which we term the keyhole frequency. As energy density further increases, the melt pool deepens, eventually leading to the formation of porosity. AE was analyzed at the onset of porosity formation, which was measured through post-mortem X-ray Computed Tomography (XCT) observations.

Figure 6 shows histograms of CWT peak frequencies at increasing laser powers, all at a constant scanning speed of 300 mm/s. The keyhole frequency, marked by a red dot on each histogram, decreases from approximately 60 kHz at the lowest power to 20 kHz at higher powers. As power–and consequently melt pool depth–increases, high-frequency components (60–80 kHz) gradually disappear (e.g., at 130 W and 140 W). However, starting from 150 W, high-frequency peaks reappear, becoming especially prominent above 300 W. Notably, porosity was first observed at 150 W and increased significantly at higher powers. 200 mm/s and 250 mm/s condition exhibited a similar pattern (see Supplementary Figure S8).

As the keyhole gets more unstable, it collapses regularly eventually leading to porosity if the entrapped gas is driven away from the vapor cavity[5,6]. High-frequency perturbative oscillations on the keyhole front wall, caused

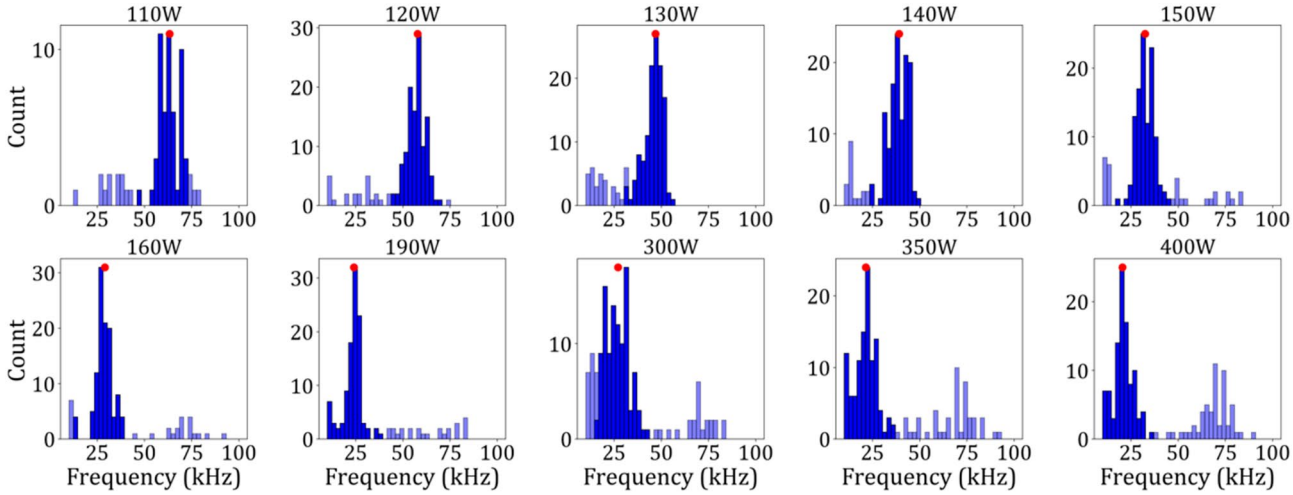

Fig. 6. Histograms of CWT peak frequencies for a constant scanning speed of 300 mm/s and increasing laser power. The keyhole frequency is indicated by a red dot, representing the median of the dark blue frequency bins. Porosity formation is first observed at the 150 W condition and persists at higher powers. Material is Ti–6Al–4V.

by liquid protrusions, have been identified to be a cause for keyhole porosity formation[17]. Protrusion occurrence is chaotic, with a high variability in frequency, reported to be above 40 kHz. These protrusions induce a transient rise in local temperature and generate a strong recoil pressure jet that exits the vapor cavity vertically, thereby destabilizing the plume oriented perpendicular to the keyhole front wall. This plume destabilization is suspected to produce the high-frequency sound observed at the corresponding oscillation frequency.

Monitoring of multi-tracks

Multi-tracks experiments were realized on bare-substrate Ti–6Al–4V plate. A simple zig-zag scanning pattern over a 10×10 mm square area was employed, using a constant hatch spacing of 50 μm. Two scans were conducted at a scanning speed of 600 mm/s, with laser powers of 160 W (referred to as M1) and 220 W (M2). Post-mortem XCT revealed high porosity formation in both cases. The porosity distribution in the M1 scan was spatially inhomogeneous, highlighting in-process instabilities.

The porosity volume was quantified via image analysis of the XCT scans and synchronized with the AE signal, as shown in Fig. 7. For the M1 condition (Fig. 7a), a relationship between porosity formation and AE amplitude is evident. However, the porosity volume does not correlate directly with the AE RMS: an increase in porosity does not always correspond to an increase in AE amplitude (e.g., between $X = 2000$–4000 μm). Nonetheless, the drop in porosity observed at $X = 4000$ μm coincides with a sudden decrease in AE RMS. Although the melting regime clearly influences AE amplitude, porosity volume cannot be predicted from AE amplitude alone. For the M2 condition (Fig. 7b), both the porosity volume and AE RMS remain stable throughout the scan.

To investigate the changes in melting conditions for the M1 scan, a cross-sectional observation was performed perpendicular to the scanning direction at the $X = 5000$ μm plane. Cross-section observation revealed the melt pool boundaries, and the melt pool depth was extracted along the X-axis. The melt pool depth was found to fluctuate significantly during the scan, ranging from approximately 100 μm in shallow regions to 200 μm in deeper areas. Notably, the shallower regions corresponded to zones with reduced porosity formation. This indicates that the melting regime alternated between deep melt pools with high porosity and shallow melt pools with lower porosity levels. Melt pool depth was found to be directly correlated with AE amplitude, as illustrated in Fig. 8. Instabilities in the melting regime can therefore be detected via airborne AE amplitude monitoring, provided they influence the melt pool depth. AE amplitude does not consistently correlate with porosity volume. While amplitude reflects melt pool dynamics, it alone cannot predict defect severity. A combined frequency-amplitude model is needed but not yet developed.

In the cross-sectional observation, the spacing between adjacent melt pools in the shallow region was measured to be 100 μm, despite the programmed hatch spacing of 50 μm. This suggests that one scanning direction in the zigzag pattern was favored, resulting in deeper melting. Conversely, in deeper regions, the hatch spacing was consistent with the programmed 50 μm, and the melt pool depth was similar for both scanning directions (see Supplementary Fig. S6). A closer examination of the AE signal in low-porosity, shallow-depth regions reveals amplitude fluctuations with a periodicity on the order of a microsecond–corresponding to the duration of a single line scan (e.g. Fig. 8, $X = 4000 - 6000$ μm). The instability of the melting regime associated with the laser scanning direction is thus also revealed by the periodicity in AE signal. Moreover, CWT analysis showed that the keyhole frequency was higher in the shallow regions and lower in the deeper regions (Supplementary Fig. S7), in agreement with the findings from the previous section. Here, the scanning strategy triggered the in process instability, most likely due to the change in angle between laser and melt pool front

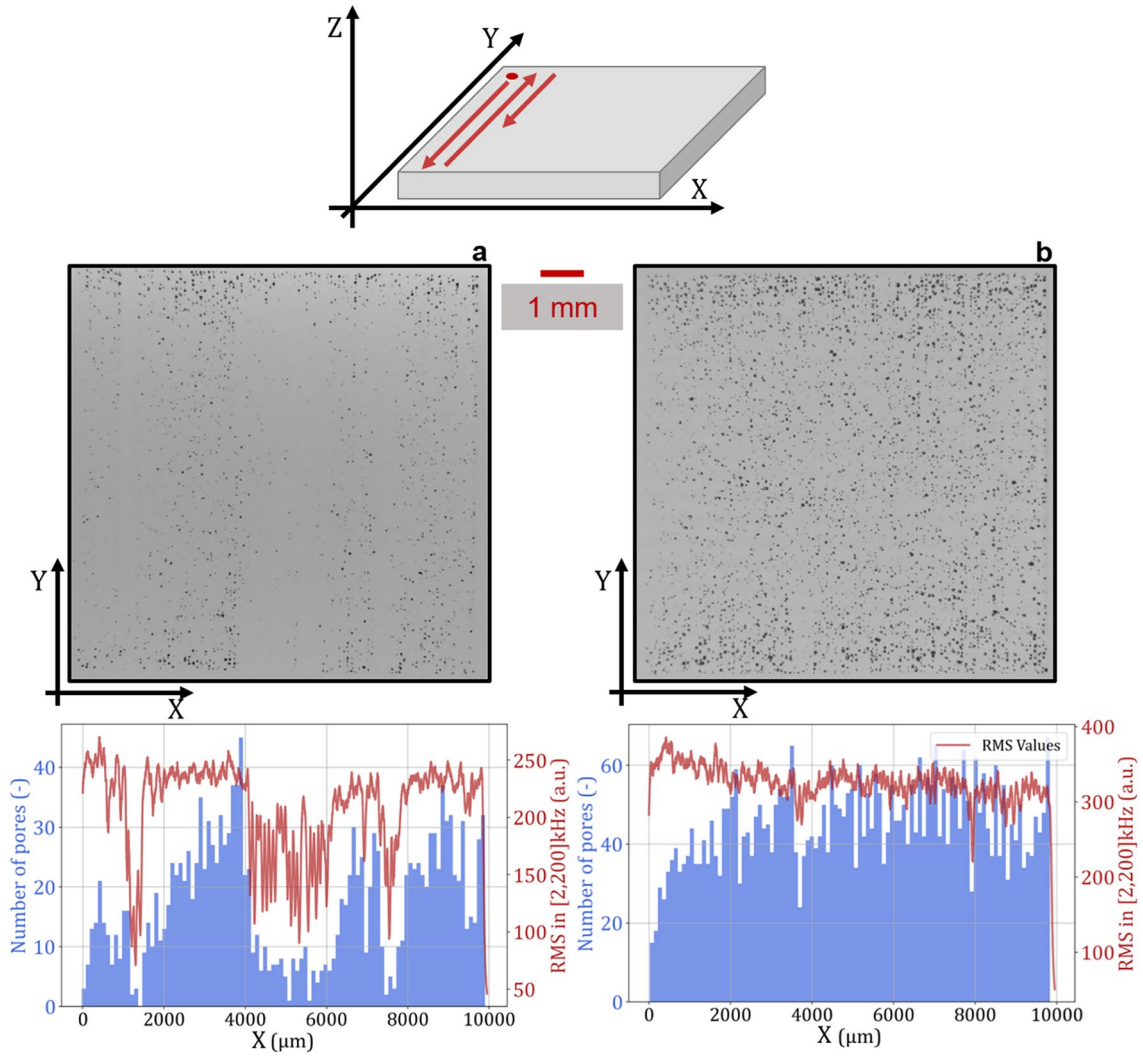

Fig. 7. Multitrack experiment XCT observation, and AE Root Mean Square (RMS) along porosity distribution determined through image analysis. **(a)** M1 condition, **(b)** M2 condition.

wall between the two scanning directions as revealed by the cross-section observation. Insights onto scanning strategy optimization and its effect on instabilities are lacking.

Conclusion

In summary, this study demonstrates airborne AE monitoring as an effective tool for observing the LPBF process. A distinct keyhole frequency was consistently detected during keyhole formation across various materials and process parameters. This frequency is inversely proportional to the depth of the vapor cavity, offering a reliable means of detecting instabilities. Unlike signal amplitude, frequency-based monitoring is largely unaffected by environmental noise, microphone sensitivity, or positioning, and remains consistent across different printers.

Evidence suggests that this frequency arises from oscillations of the rear keyhole wall, which periodically shift the vaporization site between the front and rear walls. Variations within the 15–80 kHz range correlate with melt pool depth, while the reappearance of high-frequency components (70 kHz) in deep keyholes aligns with the onset of porosity. These are attributed to chaotic protrusions on the front wall, leading to localized bursts of vaporization.

Future studies should integrate AE sensing with high-speed X-ray imaging and plume diagnostics, especially during transitions to keyhole mode and the early stages of porosity development in order to validate the link between the origin of the keyhole acoustic frequency and the keyhole oscillations.

Experiments were conducted on bare substrates, whereas actual LPBF involves powder layers. The effect of powder on AE signals and plume behavior remains unexplored, raising concerns about practical applicability. The presence of powder has a limited effect on the keyhole morphology[4]. However, plume behavior as well as dynamic behavior have however be shown to differ in powder scans[6,35], which could have an effect onto the keyhole frequency and requires further investigation.

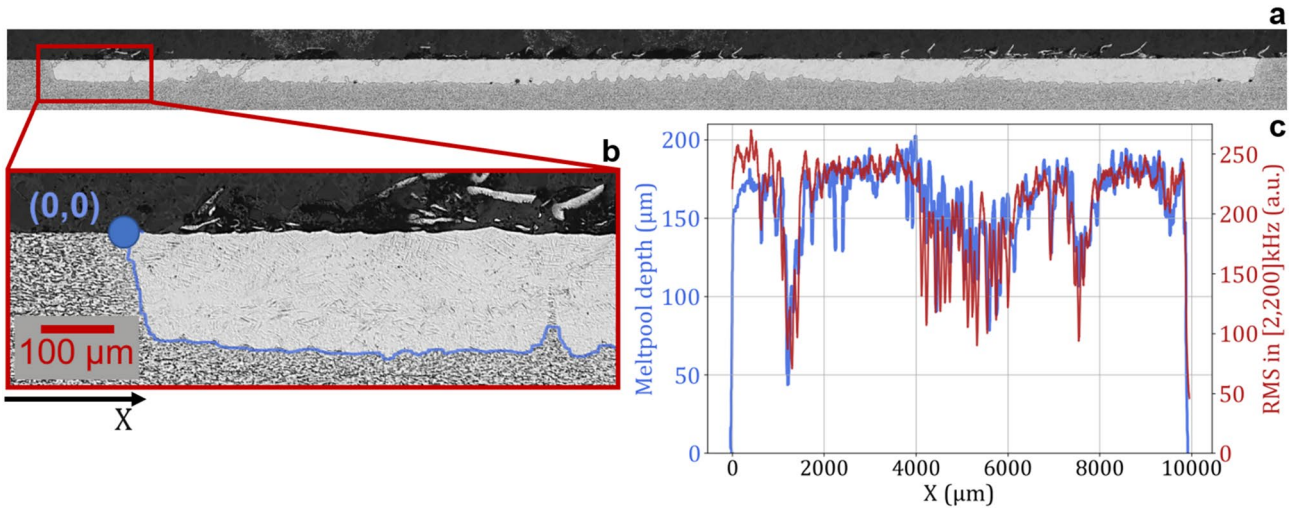

Fig. 8. **(a)** M1 cross-section observation. Melt pool horizontal length is 10 mm. **(b)** Close-up on the beginning of the cross-section. **(c)** Melt pool depth against AE RMS signal along the X-axis (perpendicular to the zig-zag pattern).

Multi-track experiments revealed a clear relationship between AE signal amplitude and the melting regime. Although amplitude-based monitoring is more sensitive to noise and setup variability, combining both amplitude and frequency information could provide a robust basis for closed-loop control or fault detection. Given that AE monitoring systems are relatively simple to integrate into existing LPBF machines, this approach offers a practical path toward enhanced process stability and quality assurance.

Methods

Materials

A Ti–6Al–4V plate with a thickness of 3 mm was used as the substrate (ASTM Gr.5, ofa titanium, Japan), S316L (5 mm thick) and Inconel625 (2 mm thick, UNS N06625, Nilaco, Japan) plates were used under bare-substrate-only conditions.

Experimental setup

Two different LPBF apparatuses were used in this study. The first was a commercial EOSINT M280 printer, equipped with a Yb-fiber laser featuring a focused D4σ diameter of approximately 100 μm at the sample surface and a maximum power output of 380 W. The chamber was filled with argon shielding gas prior to experimentation. This setup is used for multi-track experiments and cross-section, surface observation of Fig. 1.

The second setup comprised a continuous-wave laser (RFL-C500W, Raycus Fiber Technologies Co., Ltd.) and an associated galvanometer scanner (SG8230, SINOGALVO Technology Co., Ltd.), delivering a focused D4σ diameter of approximately 120 μm and a maximum power of 500 W. This setup was used for all keyhole frequency measurements as well as for the high-speed imaging experiments presented in this work.

An airborne microphone (Avisoft Bioacoustics CM16/CMPA coupled with an UltraSoundGate 116H) was used to record acoustic emission. The microphone is sensitive in the 2–200 kHz frequency range. A sampling frequency of 1 MHz was employed, allowing analysis of the entire spectrum within the microphone's sensitivity range.

Plume observation

Plume observation was performed using a high-speed camera (Phantom Miro M110) operating at 10,000 fps with an exposure time of 10 μs. Extreme Dynamic Range (EDR) functionality was employed to dynamically reduce the exposure time of overexposed pixels to 2 μs. Recording was triggered by an intensity threshold, and pre-trigger buffering allowed frames prior to the trigger event to be captured. The camera was focused on a single scan track at an angle of approximately 30° relative to the substrate surface. Due to the high intensity of the melt pool and reflections on the protective glass, basic filtering was applied to the acquired images. First, a median filter was applied across five consecutive frames to suppress transient reflections. Glare was estimated using a 51×51 pixel elliptical kernel and subsequently subtracted from the image. Finally, contours were detected using the cv2 Python library. Although some reflections remained in the filtered images, they did not affect the segmentation, which remained robust across the different conditions investigated.

XCT observation

X-ray computed tomography (XCT) was performed using a Zeiss Xradia 520 Versa 3D X-ray microscope. Pore segmentation was carried out using DragonFly software, incorporating Otsu thresholding, morphological operations, and filtering based on a minimum voxel count. The position and volume of the segmented pores were extracted for further analysis.

Cross-section observation

To observe the melt pool cross-section, specimens were sectioned perpendicular to the laser scanning direction. For mirror-surface preparation, the specimens were first mounted in epoxy resin, followed by mechanical-chemical polishing using SiC abrasive papers, a 1 μm alumina suspension, and a 50 nm SiO2 colloidal silica suspension (OP-S). Ti–6Al–4V specimens were etched with Kroll's reagent to reveal the microstructure.

Low-speed single-track experiments were observed at three different locations (0.5, 0.7, and 0.9 mm). The measured melt pool depths were averaged and plotted as a single data point. For the other conditions, melt pool depths were measured at only one location. As these refer to single points, the deep melt pools under such conditions are expected to exhibit high variability.

Supplementary Figure S9 shows the variability in melt pool depth along a track. This fluctuation gets significant for deep melt pools (around 10% relative change was measured at most).

CWT and keyhole frequency calculation

To extract salient features from the time-frequency representation of acoustic signals, we implemented a peak detection routine applied to the 2D array of CWT coefficients. The CWT was computed using python's PyWavelets[36] package. The frequency range was divided into 200 bins, evenly spaced on a logarithmic scale between 5 kHz and 200 kHz, with a temporal resolution of 1 μs. The resulting CWT is an (n, m)-sized array, where $n = 200$ and m corresponds to the signal duration in microseconds. Local maxima were identified within this array using the maximum_filter function from Python's SciPy package[37]. This method applies a maximum filter over a defined neighborhood in both time and frequency domains to locate local peaks in the CWT coefficient matrix. The neighborhood size was determined empirically and found to be robust across the entire dataset; a window of (25, 100) was used, corresponding to 25 frequency bins (log-spaced) and a 100 μs time window. A threshold of 36 dB was then applied to exclude noise-related local maxima. Following the extraction of local maxima, their frequency values were binned into a histogram spanning 10 to 100 kHz. A frequency window of ± 15 kHz around the most populated bin was then selected, and the median of this window was identified as the keyhole oscillation frequency.

This method was implemented in order to be able to track the keyhole frequency and its eventual change in time, through the change of local maxima frequency. Under stable conditions, the extracted frequency closely corresponds to a distinct peak observed in the Fast Fourier Transform (see Supplementary Figure S2).

Data availability

Supplementary data are provided with this manuscript. Additional datasets generated and/or analyzed during the current study are available from the corresponding author upon reasonable request.

Received: 4 September 2025; Accepted: 3 November 2025
Published online: 05 December 2025

References

1. Blakey-Milner, B. et al. Metal additive manufacturing in aerospace: A review. *Mater. Des.* **209**, 110008. https://doi.org/10.1016/j.matdes.2021.110008 (2021).
2. Jamróz, W., Szafraniec, J., Kurek, M. & Jachowicz, R. 3d printing in pharmaceutical and medical applications - recent achievements and challenges. *Pharm. Res.* **35**, 176. https://doi.org/10.1007/s11095-018-2454-x (2018).
3. King, W. E. et al. Observation of keyhole-mode laser melting in laser powder-bed fusion additive manufacturing. *J. Mater. Process. Technol.* **214**, 2915–2925. https://doi.org/10.1016/j.jmatprotec.2014.06.005 (2014).
4. Cunningham, R. et al. Keyhole threshold and morphology in laser melting revealed by ultrahigh-speed x-ray imaging. *Science* **363**, 849–852. https://doi.org/10.1126/science.aav4687 (2019).
5. Huang, Y. et al. Keyhole fluctuation and pore formation mechanisms during laser powder bed fusion additive manufacturing. *Nat. Commun.* **13**, 1170. https://doi.org/10.1038/s41467-022-28694-x (2022).
6. Zhao, C. et al. Critical instability at moving keyhole tip generates porosity in laser melting. *Science* **370**, 1080–1086. https://doi.org/10.1126/science.abd1587 (2020).
7. Martin, A. A. et al. Dynamics of pore formation during laser powder bed fusion additive manufacturing. *Nat. Commun.* **10**, 1987. https://doi.org/10.1038/s41467-019-10009-2 (2019).
8. Gan, Z. et al. Universal scaling laws of keyhole stability and porosity in 3d printing of metals. *Nat. Commun.* **12**, 2379. https://doi.org/10.1038/s41467-021-22704-0 (2021).
9. Ye, J. et al. Energy coupling mechanisms and scaling behavior associated with laser powder bed fusion additive manufacturing. *Adv. Eng. Mater.* **21**, 1900185. https://doi.org/10.1002/adem.201900185 (2019).
10. Fabbro, R. Scaling laws for the laser welding process in keyhole mode. *Journal of Materials Processing Technology***264**, https://doi.org/10.1016/j.jmatprotec.2018.09.027 (2018).
11. Hamidi Nasab, M. et al. Harmonizing sound and light: X-ray imaging unveils acoustic signatures of stochastic inter-regime instabilities during laser melting. *Nat. Commun.* **14**, 8008. https://doi.org/10.1038/s41467-023-43371-3 (2023).
12. Chen, Q. et al. Elucidating the effect of preheating temperature on melt pool morphology variation in inconel 718 laser powder bed fusion via simulation and experiment. *Addit. Manuf.* **37**, 101642. https://doi.org/10.1016/j.addma.2020.101642 (2021).
13. Mishurova, T. et al. Understanding the hot isostatic pressing effectiveness of laser powder bed fusion Ti–6Al–4V by in-situ x-ray imaging and diffraction experiments. *Sci. Rep.* **13**, 18433. https://doi.org/10.1038/s41598-023-45258-1 (2023).
14. Taherkhani, K., Sheydaeian, E., Eischer, C., Otto, M. & Toyserkani, E. Development of a defect-detection platform using photodiode signals collected from the melt pool of laser powder-bed fusion. *Addit. Manuf.* **46**, 102152. https://doi.org/10.1016/j.addma.2021.102152 (2021).
15. Lu, Q., Grasso, M., Le, T.-P. & Seita, M. Predicting build density in l-pbf through in-situ analysis of surface topography using powder bed scanner technology. *Addit. Manuf.* **51**, 102626. https://doi.org/10.1016/j.addma.2022.102626 (2022).
16. Estalaki, S. M., Lough, C. S., Landers, R. G., Kinzel, E. C. & Luo, T. Predicting defects in laser powder bed fusion using in-situ thermal imaging data and machine learning. *Addit. Manuf.* **58**, 103008. https://doi.org/10.1016/j.addma.2022.103008 (2022).
17. Ren, Z. et al. Machine learning–aided real-time detection of keyhole pore generation in laser powder bed fusion. *Science* **379**, 89–94. https://doi.org/10.1126/science.add4667 (2023).

18. Shevchik, S., Kenel, C., Leinenbach, C. & Wasmer, K. Acoustic emission for in situ quality monitoring in additive manufacturing using spectral convolutional neural networks. *Addit. Manuf.* **21**, 598–604. https://doi.org/10.1016/j.addma.2017.11.012 (2018).
19. Authier, N. et al. Coupled membrane free optical microphone and optical coherence tomography keyhole measurements to setup welding laser parameters. In Kaierle, S. & Heinemann, S. W. (eds.) *High-Power Laser Materials Processing: Applications, Diagnostics, and Systems IX*, vol. 11273, 1127308, https://doi.org/10.1117/12.2543999. International Society for Optics and Photonics (SPIE, 2020).
20. Ito, K., Kusano, M., Demura, M. & Watanabe, M. Detection and location of microdefects during selective laser melting by wireless acoustic emission measurement. *Addit. Manuf.* **40**, 101915. https://doi.org/10.1016/j.addma.2021.101915 (2021).
21. Sun, Y. et al. Direct mechanistic connection between acoustic signals and melt pool morphology during laser powder bed fusion. *Appl. Phys. Lett.* **125**, 034102. https://doi.org/10.1063/5.0205663 (2024) https://pubs.aip.org/aip/apl/article-pdf/doi/10.1063/5.0205663/20048858/034102_1_5.0205663.pdf.
22. *Non-contact acoustic emission monitoring during laser processing*, vol. ICALEO '92: Proceedings of the Laser Materials Processing Symposium of *ICALEO*. https://doi.org/10.2351/1.5058543. https://pubs.aip.org/icaleo/proceedings-pdf/ICALEO92/1992A/719/20067321/ica.v1992.i1.719_1.online.pdf.
23. Klein, T., Vicanek, M. & Simon, G. Forced oscillations of the keyhole in penetration laser beam welding. *J. Phys. D Appl. Phys.* **29**, 322. https://doi.org/10.1088/0022-3727/29/2/008 (1996).
24. Yuan, W. et al. Oscillatory nature in melt-gas-powder interactions during laser powder bed fusion process revealed by cfd-dem coupled modelling. *Virtual Phys. Prototyping* **20**, e2446619. https://doi.org/10.1080/17452759.2024.2446619 (2025).
25. Khairallah, S. A., Sun, T. & Simonds, B. J. Onset of periodic oscillations as a precursor of a transition to pore-generating turbulence in laser melting. *Additive Manuf. Letters* **1**, 100002. https://doi.org/10.1016/j.addlet.2021.100002 (2021).
26. Chan, C., Mazumder, J. & Chen, M. M. A two-dimensional transient model for convection in laser melted pool. *Metall. Trans. A* **15**, 2175–2184. https://doi.org/10.1007/BF02647100 (1984).
27. Li, E., Zhou, Z., Wang, L., Zou, R. & Yu, A. Modelling of keyhole dynamics and melt pool flow in laser powder bed fusion process. *Powder Technol.* **400**, 117262. https://doi.org/10.1016/j.powtec.2022.117262 (2022).
28. Brock, C., Hohenstein, R. & Schmidt, M. Mechanisms of vapour plume formation in laser deep penetration welding. *Opt. Lasers Eng.* **58**, 93–101. https://doi.org/10.1016/j.optlaseng.2014.02.001 (2014).
29. Reese, Z., Fox, J., Evans, C. & Taylor, J. Evolution of cooling length in parts created through laser powder bed fusion additive manufacturing (2018).
30. Fabbro, R. & Chouf, K. Keyhole modeling during laser welding. *Journal of Applied Physics***87**, 4075–4083, https://doi.org/10.1063/1.373033 (2000). https://pubs.aip.org/aip/jap/article-pdf/87/9/4075/19169423/4075_1_online.pdf.
31. Aune, R. et al. Surface tension and viscosity of industrial alloys from parabolic flight experiments - results of the thermolab project. *Microgravity - Sci. Technol.* **16**, 11–14. https://doi.org/10.1007/BF02945937 (2005).
32. Valencia, J. J. & Peter, N. Q. Thermophysical properties. In *ASM Handbook, Volume 15: Casting*, 468–481 (ASM International, 2008).
33. Pichler, P., Leitner, T., Kaschnitz, E., Rattenberger, J. & Pottlacher, G. Surface tension and thermal conductivity of nist srm 1155a (aisi 316l stainless steel). *Int. J. Thermophys.* **43**, 66. https://doi.org/10.1007/s10765-022-02991-5 (2022).
34. Metelkova, J. et al. On the influence of laser defocusing in selective laser melting of 316l. *Addit. Manuf.* **23**, 161–169. https://doi.org/10.1016/j.addma.2018.08.006 (2018).
35. Bitharas, I. et al. The interplay between vapour, liquid, and solid phases in laser powder bed fusion. *Nat. Commun.* **13**, 2959. https://doi.org/10.1038/s41467-022-30667-z (2022).
36. Lee, G. R., Gommers, R., Waselewski, F., Wohlfahrt, K. & OĹeary, A. Pywavelets: A python package for wavelet analysis. *J. Open Source Softw.* **4**, 1237. https://doi.org/10.21105/joss.01237 (2019).
37. fundamental algorithms for scientific computing in python. Virtanen, P. et al. Scipy 1.0. *Nature Methods***17**, 261–272. https://doi.org/10.1038/s41592-019-0686-2 (2020).

Author contributions

L.G., F.B. and H.M. conceived the experiments. L.G., F.B., H.M. and K.I. conducted the experiments. L.G. analyzed the results and wrote the manuscript. M.W., T.S., and M.E. provided resources, secured funding, and oversaw project administration. All authors contributed to and reviewed the final manuscript.

Funding

This work was supported by JSPS KAKENHI Grant-in-Aid for Transformative Research Areas (A) (Grant Number 24H00982). Financial support from the Council for Science, Technology, and Innovation (CSTI), Cross-ministerial Strategic Innovation Promotion Program (SIP), "Materials Integration for revolutionary design system of structural materials" (Funding agency: JST) is gratefully acknowledged. The research was conducted while the first author was supported by the MEXT Scholarship.

Declarations

Competing interests

The authors declare that they have no competing interests.

Additional information

Supplementary Information The online version contains supplementary material available at https://doi.org/10.1038/s41598-025-27232-1.

Correspondence and requests for materials should be addressed to L.G.